arXiv:astro-ph/0202139v2 30 Aug 2002

On the Asymmetries of Extended X-ray Emission from Planetary Nebulae

Joel H. Kastner[1], Jingqiang Li[1], Saku D. Vrtilek[2], Ian Gatley[1], K. M. Merrill[3], and Noam Soker[4]

1. Chester F. Carlson Center for Imaging Science, Rochester Institute of Technology, 54 Lomb Memorial Dr., Rochester, NY 14623; JHK's email: jhk@cis.rit.edu

2. Harvard-Smithsonian Center for Astrophysics, Cambridge, MA 02138; saku@cfa.harvard.edu

3. National Optical Astronomy Observatories, Tucson, AZ; merrill@noao.edu

4. Department of Physics, Oranim, Tivon 36006, ISRAEL; soker@physics.technion.ac.il

Received _____; accepted _____

ABSTRACT

Chandra X-ray Observatory (CXO) images have revealed that the X-ray emitting regions of the molecule-rich young planetary nebulae (PNs) BD +30°3639 and NGC 7027 are much more asymmetric than their optical nebulosities. To evaluate the potential origins of these X-ray asymmetries, we analyze X-ray images of BD +30°3639, NGC 7027, and another planetary nebula resolved by CXO, NGC 6543, within specific energy bands. Image resolution has been optimized by sub-pixel repositioning of individual X-ray events. The resulting subarcsecond-resolution images reveal that the soft ($E < 0.7$ keV) X-ray emission from BD +30°3639 is more uniform than the harder emission, which is largely confined to the eastern rim of the optical nebula. In contrast, soft X-rays from NGC 7027 are highly localized and this PN is more axially symmetric in harder emission. The broad-band X-ray morphologies of BD +30°3639 and NGC 7027 are highly anticorrelated with their distributions of visual extinction, as determined from high-resolution, space- and ground-based optical and infrared imaging. Hence, it is likely that the observed X-ray asymmetries of these nebulae are due in large part to the effects of nonuniform intranebular extinction. However, the energy-dependent X-ray structures in both nebulae and in NGC 6543 — which is by far the least dusty and molecule-rich of the three PNs, and displays very uniform intranebular extinction — suggests that other mechanisms, such as the action of collimated outflows and heat conduction, are also important in determining the detailed X-ray morphologies of young planetary nebulae.

Subject headings: stars: mass loss — stars: winds, outflows — planetary nebulae: individual (BD +30°3639, NGC 7027, NGC 6543) — X-rays: ISM

1. Introduction

Models of the formation of PNs have long predicted that these objects, representing very late stages in the deaths of intermediate-mass (1-8 $M_{\odot}$) stars, should emit X-rays. Such emission should arise in shocks at the interface between an active wind from the PN core (or its companion) and material ejected when the progenitor was on the asymptotic giant branch (AGB). Thus, extended X-ray emission, if present, likely traces the very processes responsible for sculpting PNs (for recent discussions of PN shaping mechanisms see, e.g., Frank 1999; Gardiner & Frank 2001; Kastner, Soker, & Rappaport 2000a; and Soker & Rappaport 2000).

The Chandra X-ray Observatory (CXO), with its unprecedented spatial resolution, has now provided the first conclusive evidence of such extended X-ray emission from nebular gas, in the form of striking X-ray imagery of the young PNs BD +30°3639 (Kastner et al. 2000b, hereafter KSVD), NGC 7027 (Kastner, Vrtilek, & Soker 2001, hereafter KVS), and NGC 6543 (Chu et al. 2001). Observations of the PN NGC 7009 by XMM-Newton, which combines high sensitivity with good spatial and spectral resolution, also reveal marginally extended X-ray emitting gas (Guerrero, Chu, & Gruendl 2002). The PN NGC 7293 (the Helix), known to exhibit relatively hard X-ray emission, does not display evidence for extended emission in CXO imaging (Guerrero et al. 2001); instead, this PN and NGC 6543 contain point-like X-ray sources with temperatures of a few times 10^6 K, possibly due to magnetic activity on companions to their central stars (Guerrero et al. 2001; Gruendl et al. 2001; Soker & Kastner 2002).

While revealing the diffuse nature of the X-ray emission from some PNs, these first CXO and XMM-Newton observations of PNs are notable and surprising in several respects. Of particular interest is the result that the X-ray morphologies of the young PNs BD +30°3639 and NGC 7027 are decidely asymmetric, much more so than their optical nebulosities.

Although the extended emission detected in the CXO images of these PNs (and NGC 6543 and 7009) underscores the importance of strong shocks in shaping planetaries, the asymmetric structures observed by CXO in BD +30°3639 and NGC 7027 cannot be easily explained in terms of "fossil," spherical AGB envelopes acted on by isotropic white dwarf winds. However, as BD +30°3639 and NGC 7027 are also among the youngest, dustiest, and most molecule-rich of known PNs, it is important to assess the extent to which their observed X-ray asymmetries represent intrinsic plasma density or temperature structure inhomogeneities rather than, e.g., the effects of intervening X-ray absorption.

In this paper, we explore the origin of asymmetries of extended X-ray emission from PNs (in a companion paper, Soker & Kastner 2003, we examine models to explain the observed X-ray luminosities and temperatures of PNs). In particular, we consider the role of nonuniform intranebular extinction in determining the X-ray morphologies of BD +30°3639, NGC 7027, and NGC 6543. In doing so, we take advantage of the subarcsecond imaging potential of CXO and the energy resolution of CXO's Advanced CCD Imaging Spectrometer (ACIS). In §2 we present archival optical and near-infrared images of BD +30°3639 and NGC 7027 that are useful in deducing their distributions of intranebular extinction, and we summarize the application of a sub-pixel image restoration technique to CXO images of these nebulae and NGC 6543. Results, including presentation of super-resolved, energy-band images of all three PNs and comparisons of their X-ray surface brightnesses and spatial distribution of intranebular extinction (as inferred from the optical/near-IR data), are presented in §3. In §4, we discuss our main findings, and §5 contains a summary.

2. Observations and data processing

2.1. Optical and Infrared

Images of BD +30°3639 in the transitions of Hα (0.6563 μm) and Pα (1.87 μm) utilized in the present analysis (§3) were obtained with the *Hubble Space Telescope* using the WFPC2 and NICMOS cameras, respectively. These images appear in Fig. 1. The Hα and Pα images were first presented in Sahai & Trauger (1998) and Latter et al. (2000a), respectively; in addition, HST narrow-band images covering many diagnostic emission lines were presented in Arnaud et al. (1996) and Harrington et al. (1997). The reader is referred to these papers for details concerning the structure and physical conditions of BD +30°3639 as ascertained from HST imaging. As is readily apparent from Fig. 1, however, the inner nebula consists of a bright elliptical shell with major and minor axes of $\sim 4''$ and $\sim 3''$, respectively (this inner nebula is surrounded by a much larger, fainter Hα halo; Sahai & Trauger 1998). There is a strong gradient in extinction across this region of the nebula, with many conspicuous knots and clumps of denser gas apparent in projection against the bright elliptical shell (Harrington et al. 1997).

Images of NGC 7027 in the transitions of Brγ (2.16 μm) and Brα (4.05 μm) utilized in the present analysis (§3) were obtained with the National Optical Astronomy Observatories[1] 4 m telescope and Cryogenic Optical Bench (COB) at Kitt Peak National Observatory in 1995 September (for details concerning COB imaging on the 4 m, see Weintraub et al. 1996). These images appear in Fig. 2. Like BD +30°3639, NGC 7027 displays a bright, elliptical shell, with a fainter surrounding halo; the major and minor axes of the shell are

[1]National Optical Astronomy Observatory is operated by the Association of Universities for Research in Astronomy, Inc. (AURA), under cooperative agreement with the National Science Foundation.

$\sim 10''$ and $\sim 7''$, respectively. While extensive near-infrared imagery of NGC 7027 has been obtained in the 2–3 μm wavelength range (e.g., Graham et al. 1993; Kastner et al. 1994, 1996; Latter et al. 2000b; Cox et al. 2002), the Brα image presented here represents the longest wavelength image of the nebula presently available at $\sim 1''$ resolution. As we demonstrate in §4, this image is valuable for examining, at high spatial resolution, highly obscured regions of the nebula.

2.2. X-ray

BD +30°3639 and NGC 7027 were observed by CXO in 2000 March and 2000 June, with net integration times of 18.8 ks and 18.2 ks, respectively. Both PNs were imaged with the central back-illuminated CCD in the ACIS array (ACIS-S3). These observations were first presented in KSVD and KVS. NGC 6543 was observed with ACIS-S3 for 46.0 ks in 2000 May (Chu et al. 2001). In this paper, we make use of these CXO/ACIS-S3 event data as reprocessed by the Chandra X-ray Center (CXC) in 2000 December for BD +30°3639 and in 2001 January for NGC 7027 and NGC 6543 (Figs. 3, 4, & 5, respectively).

2.2.1. Event position refinement

The FWHM of the core of the point spread function (PSF) of the CXO High Resolution Mirror Assembly (HRMA) is nearly equivalent to the ACIS-S3 pixel size, $0.49''$.[2] Because (1) the telescope position is dithered across the source during an observation and is known

[2]See Chandra X-ray Observatory Proposer's Guide, V. 4 (http://cxc.harvard.edu/udocs/docs/POG/MPOG/index.html), §5.4.

to an accuracy of better than 0.3″,[3] (2) the charge cloud size generated by an incident photon is much smaller than the ACIS pixel size (Tsunemi et al. 2001), and (3) the ACIS flight software records the distibution of charge among pixels for each candidate X-ray event (encoded as "FLTGRADE," the bitmap value of pixels above the "split threshold"[4]), it is possible (in principle) to reconstruct the position of each detected X-ray to sub-pixel accuracy (e.g., Tsunemi et al.). We have thus applied event position corrections to the reprocessed data obtained for BD +30°3639, NGC 7027, and NGC 6543, following the general method outlined in Tsunemi et al., as implemented, refined, and tested by Li et al. (2002). That is, we move the position of a photon from the default (pixel center) to its inferred landing location in detector coordinates, according to the event grade (see below). We then use the telescope pointing and spacecraft roll angle history for the observation to project the revised event locations to sky coordinates.

The Tsunemi et al. (2001) method relies on rejection of all events except those with charge distributed among three or four pixels; these "corner split" events have better sub-pixel accuracy in both directions (horizontal and vertical) than single events and in one direction than two-pixel events, thereby maximizing the potential improvement in spatial resolution. However, corner splits constitute only about 10% of the total number of events for a typical ACIS-S3 observation of a soft source (e.g., Table 1). Thus, to boost the signal-to-noise ratio, Li et al. (2002) include single-pixel as well as two-pixel events for which the charge is split either horizontally or vertically. As we demonstrate below, the improvement in image quality remains significant for this more inclusive FLTGRADE selection. In calculating new photon landing positions in detector coordinates, Li et al. assume single pixel events correspond to photons absorbed at the event pixel center, 2-pixel

[3]Chandra X-ray Observatory Proposer's Guide, V. 4, §4.2.3.

[4]Chandra X-ray Observatory Proposer's Guide, V. 4, §6.3.

vertical or horizontal split event photons land at the centers of the split boundaries, and the corner split event photons land at the split corners. Before applying this event position relocation algorithm, position randomization within an ACIS pixel (performed as part of the standard CXC event processing pipeline) must be reversed.

In Table 1 we summarize the event FLTGRADE distributions for BD +30°3639, NGC 7027, and NGC 6543. In compiling these statistics we have selected those events with nominal energies < 3.0 keV (as determined from calibrations produced by the standard CXC ACIS processing pipeline) that lie within the BD +30°3639, NGC 7027, and NGC 6543 source regions as defined in KVS, KSVD, and Chu et al. 2001, respectively. It can be seen that our event selection criteria retain $\geq 95\%$ of events in the source regions (the selected events necessarily include a small percentage of background events).

3. Results

3.1. Sub-pixel image reconstruction

Results of application of subpixel event relocations to the PN event data are displayed in Figs. 3, 4, and 5. In each Figure, the original image — i.e., the image obtained by spatially binning the Level 1 event data provided via standard event processing by the CXC, after filtering on energy and FLTGRADE (§2.2.1) — is presented in the left-hand panel. Images constructed from "unrandomized" event positions are displayed in the center panels of each Figure; in both these unrandomized images and in the "original" images constructed from Level 1 events, the pixel size is set to the intrinsic pixel size of ACIS, 0.49″. Finally, the right-hand panels of each Figure display images constructed after relocating events according to the subpixel event repositioning algorithm. These images were constructed for a pixel size of 0.25″, which fully samples the HRMA PSF at the energy range characteristic

of the three PNs (0.3 keV to 3.0 keV).

The comparisons between "original," "unrandomized," and "event relocated" images in Figs. 3, 4, and 5 illustrate the superior spatial resolution afforded by subpixel event repositioning. Perhaps the best example of such an improvement is the sharply decreased FWHM of the central point source in NGC 6543 (compare the left- and right-hand panels of Fig. 5): before correction we measure a FWHM of 1.12″, and after correction we measure a FWHM of 0.80″. Similarly, after event relocation is applied, the X-ray outline of BD +30°3639 and the bright region of emission at its eastern edge appear sharper (Fig. 3, right). The number of counts per pixel is quite small in the reconstructed image of NGC 7027, so some of the structure in this image is due to small number statistics. Nevertheless, features in the brighter regions of these images (e.g., the compact, bright region located northwest of the position of the central star) appear to correspond to features seen in optical and near-infrared images of this PN (§§3.2, 3.3).

The absolute astrometry of the reprocessed BD +30°3639 and NGC 7027 data is improved over that available to KSVD and KVS, due to refined aspect solutions. Hence we can use the reconstructed images of these nebulae to re-examine the correspondence of their X-ray and optical emitting regions. For BD +30°3639, the relative alignment of the Pα image and the broad-band (0.3-3.0 keV) reconstructed image constructed from the reprocessed CXO event data agrees to within $\sim 0.5''$, based on comparison of the outlying CXO image contours with the elliptical shell seen in Pα (Fig. 6). For NGC 7027, we have adjusted the position of the X-ray image by $\sim 1''$, to better align the positions of broad-band peak X-ray surface brightness with the bright elliptical shell in the Brα image (Fig. 7). The resulting overlays of reconstructed broad-band X-ray images on infrared images (Figs. 6, 7) indicate that (a) the central stars of both PNs are confirmed to lie very near the center of their X-ray nebulosities, and (b) unlike both NGC 7293 and NGC 6543 (Guerrero et al.

2001), neither BD +30°3639 nor NGC 7027 clearly contains an X-ray-bright central star (a possibility left open for NGC 7027 by the preliminary analysis of KVS).

3.2. Energy-resolved images

In Figs. 8, 9, and 10 we present, respectively, broad-band and energy-resolved images of BD +30°3639, NGC 7027, and NGC 6543. The energy-resolved images span the energy ranges $E \leq 0.7$ keV (hereafter "soft-band"), 0.7 keV $< E \leq 1.2$ keV ("medium-band"), and 1.2 keV $< E \leq 3.0$ keV ("hard-band"). Like the broad-band images, the energy-resolved images also have been reconstructed at sub-pixel resolution, with $0.25''$ pixels, via the algorithm described in the previous section. Our analysis of the sub-pixel event positioning algorithm suggests that the results of the algorithm are robust, regardless of the count rate of the source, since the algorithm operates on one photon at a time (Li et al. 2002). Hence, the subpixel reconstructions are reliable, despite the small number of counts (and, hence, low signal-to-noise ratio) in certain energy-resolved images (e.g., hard-band images of BD +30°3639 and NGC 6543, and all images of NGC 7027).

The results demonstrate that the diffuse X-ray emission morphologies of all three nebulae are highly energy-dependent within the 0.3-3.0 keV band. In all four images of BD +30°3639 it is apparent that the X-ray emission is brightest toward its eastern rim (Fig. 8); however, this asymmetry is much more profound in the medium- and hard-band images than in the soft-band image. In the soft-band image, the peak of the surface brightness of BD +30°3639 lies close to (though $\sim 1''$ east of) the position of the central star, while in the medium- and hard-band images, the nebula is much less centrally peaked. In these images, the (clumpy) emission from just inside the rims of the optical nebula appears generally stronger than the emission from the core region, and there is a compact bright region at the eastern rim.

In contrast to BD +30°3639, the soft-band emission from NGC 7027 is highly localized (Fig. 9). This emission is entirely confined to a region in the northwest of the nebula that appears as a "hole" in high-resolution optical images (see, e.g., Fig. 1 of KVS). Emission from the X-ray-emitting "lobe" projected northwest of the central star — a direction corresponding to blueshifted atomic and molecular gas (Cox et al. 2002) — dominates the nebula in both the soft- and medium-band images. In the hard-band image the emission is more balanced between the northwest (forward-facing) and southeast (rearward-facing) X-ray lobes, and the northwest X-ray lobe has a smaller opening angle than in the medium-band image. The outline of NGC 7027 in this hard-band image appears more or less axisymmetric or, perhaps, point-symmetric.

Fig. 10 demonstrates that all diffuse X-ray emission detected from NGC 6543 emerges at energies < 1.2 keV; only the central star is detected in the hard-band image. This is consistent with the spectral analysis in Chu et al. (2001) and Guerrero et al. (2001), which indicates that the diffuse emission has a characteristic temperature $\sim 10^6$ K, while the unresolved central source is somewhat hotter, at $\sim 2 \times 10^6$ K. In the medium-band image, the emission appears confined to the edges of the soft-band nebulosity, with a clump of brighter emission at the extreme northern edge of the X-ray-emitting region.

3.3. X-ray Surface Brightness vs. Optical/IR Extinction

Assuming Case B recombination, the hydrogen emission line ratios $I_{H\alpha}/I_{P\alpha}$ and $I_{Br\gamma}/I_{Br\alpha}$ are relatively insensitive to temperature in the regime of interest for planetary nebulae, $T \sim 10^4$ K (e.g., Osterbrock 1989, Table 4.2). Therefore, we can assume that deviations of the observed line ratios from their "canonical" Case B recombination values are due to extinction. Hence, assuming a standard interstellar dependence of extinction on wavelength (e.g., Osterbrock 1989, Table 7.2), we use the spatial distribution of the ratios

$I_{H\alpha}/I_{P\alpha}$ and $I_{Br\gamma}/I_{Br\alpha}$, as derived from the ratios of images presented in §2.2, to infer visual extinction (A_V) as a function of position within BD +30°3639 (Fig. 11) and NGC 7027 (Fig. 12), respectively.

Harrington et al. (1997) and Robberto et al. (1993) employed techniques similar to the preceding, to infer the spatial distribution of A_V for BD +30°3639 and NGC 7027, respectively. Their results are qualitatively similar to those derived here. The extinction across both nebulae can be quite large, however, and use of near-infrared images provides a better "lever arm" for deducing A_V in very highly obscured regions. For example, the Robberto et al. extinction map of NGC 7027, constructed from optical hydrogen recombination line imaging, is limited to regions with $A_V < 5$, whereas the A_V map constructed from longer-wavelength hydrogen transitions available to COB (Fig. 12) remains sensitive to $A_V \sim 15$.

The distributions of A_V are similar for the two nebulae, in that the largest values of extinction lie near the nebular perimeters, and extinction "holes" are observed toward the nebular interiors. Generally, however, we find A_V within NGC 7027 (for which A_V lies largely between the range $1.5 \lesssim A_V \lesssim 15$) to be a factor 3-4 larger than A_V within BD +30°3639 (for which $0.5 \lesssim A_V \lesssim 5$). Also, the dark lane apparent in high-resolution optical images of NGC 7027 (e.g. KVS, their Fig. 1) appears as an enhancement of A_V in Fig. 12. This is consistent with the hypothesis (KVS) that BD +30°3639 and NGC 7027 share a common structure — bipolar, with a dense equatorial region — but that NGC 7027 is viewed at intermediate inclination angle whereas BD +30°3639 is viewed nearly pole-on.

Notably, the X-ray surface brightnesses of both nebulae are strongly anticorrelated with the local value of A_V. In each case, the peak of X-ray emission lies very near the minimum in A_V, and little or no X-ray emission is observed toward regions of highest A_V. There is a gradient of A_V in interior regions of BD +30°3639 (i.e., regions of the

nebula interior to the bright shell seen in H recombination lines), such that there is greater extinction toward the southwestern side of the central star (a result independently obtained by Harrington et al. 1997), and there is an extinction "hole" 1-2″ to the eastern side of the central star. The X-ray emission, correspondingly, is much brighter to the east than to the west of the star and, furthermore, the contours of X-ray surface brightness closely follow the A_V distribution in detail (Fig. 11). In NGC 7027, the relationship between A_V and X-ray surface brightness is also strong, with the lowest contours of X-ray emission very closely tracing the regions of large A_V (Fig. 12). In particular, the "pinched waist" apparent in the X-ray emission morphology lies at the position of the enhancement of A_V that appears to define the equatorial plane of the nebula. Also, the strongest X-ray emission from NGC 7027 lies very near — though slightly farther from the central star than — the extinction "hole" apparent to the northwest of the star.

We have also constructed an Hα/Hβ line ratio map of NGC 6543 (not shown), from image data available in the HST archive. In stark constrast to the line ratio maps of BD +30°3639 and NGC 7027, from which the A_V maps in Figs. 11, 12 and were constructed, the H II line ratio map of NGC 6543 is smooth and featureless across its central, X-ray-emitting region, indicating that any extinction of the X-ray nebula is quite spatially uniform. Furthermore, the measured Hα/Hβ ratio across this region, 2.5 ± 0.3, agrees within uncertainty with the value expected for Case B recombination, ~ 2.8 (Osterbrock 1989). This result is consistent with the very small inferred extinction toward NGC 6543 as measured by Tylenda et al. (1992) and with the observation that X-ray absorption becomes detectable by CXO only for energies < 0.4 keV (Chu et al. 2001).

4. Discussion

The comparisons of X-ray and extinction images in the preceding section reveal striking correspondences between the spatial distributions of A_V and the X-ray surface brightnesses of BD +30°3639 and NGC 7027. These results suggest that intranebular extinction plays a very important role in determining the X-ray emission morphologies of young, dusty PNs. The close correspondence of regions of low extinction and bright X-ray emission in both BD +30°3639 and NGC 7027 suggests that some extended X-ray emission may remain undetected, making it difficult to draw conclusions as to the intrinsic shape (e.g., axisymmetric vs. elliptically symmetric) of their soft X-ray emitting regions.

Extinction alone cannot fully explain the strong departures from spherical symmetry and small-scale clumping of the X-ray emission from all three nebulae, however. If extinction were the sole contributor to the X-ray asymmetries of BD +30°3639 and NGC 7027, then we would expect these asymmetries to be more extreme at lower energy, where photons are easily absorbed, than at higher energy, where the X-rays are more highly penetrating. By way of analogy, we note that the near-infrared emission-line morphologies of both nebulae are substantially more symmetric and regular than their optical emission-line morphologies, a difference that can be ascribed to the large decrease in the probability of scattering or absorption of photons by intranebular dust in the near-infrared, relative to the optical regime.

In the X-ray imagery presented here, however, only NGC 7027 seems to display the expected trend of increasing symmetry with increasing energy — although even at high energy, its X-ray morphology differs sharply from its shell-like appearance in near-infrared emission-line images (Fig. 7). BD +30°3639 is observed to become clumpier and more one-sided as X-ray energy increases. The hard-band emission from NGC 6543, for which extinction effects are negligible in the bands considered here, is mostly confined to a small

region of the north lobe. It seems, therefore, that strongly position-dependent variations in the physical conditions in the shocked gas are responsible, at least in part, for the asymmetric and/or clumpy X-ray-emitting regions of these PNs. Indeed, while it seems likely that intranebular extinction modulates the nebular X-ray surface brightnesses of BD +30°3639 and NGC 7027, we cannot as yet rule out other interpretations. For example, the regions of brightest X-ray emission may correspond to the smallest A_V because the dust in these regions is being destroyed by the intense, high-energy radiation.

Soker & Kastner (2003) argue that the X-ray luminosities and temperatures of PNs can be explained by a model in which the diffuse emission is produced by a shocked, moderate speed ($\sim$ 500 km s^{-1}) post-AGB wind, or a wind emanating from a companion to the central post-AGB star, where the shocked gas has had time to expand and cool adiabatically. This wind and the distribution of previously ejected AGB material also should largely determine the spatial distribution of the X-ray emitting gas. The post-AGB or companion wind may be highly collimated, resulting in strong axial or point symmetries observable in X-rays. Other processes might then govern the temperature structure (and therefore spatial distribution) of X-ray-emitting gas in detail, with heat conduction from shock-heated to photoionized gas in the presence of magnetic fields and/or direct mixing of shock-heated and photoionized gas being the most likely candidates (Soker & Kastner 2003, and references therein). These temperature-moderating mechanisms may be more or less important in different nebulae.

The images presented here, combined with the global X-ray properties of PNs displaying diffuse X-ray emission (Soker & Kastner 2003, their Table 1), support this general model. That is, adiabatic cooling of a shocked, moderate-speed, post-AGB or companion wind should produce X-ray luminosities and temperatures in the general range observed ($\sim 10^{32}$ ergs s^{-1} and $1 - 3 \times 10^6$ K, respectively). The detailed X-ray surface

brightness distributions of NGC 6543 and NGC 7027 suggest, moreover, that collimated outflows are responsible for the detailed structure of their X-ray emitting regions.

In NGC 7027, which exhibits collimated outflows in near-infrared line emission (Cox et al. 2002), the action of such a highly directed (bipolar) fast wind from the central star — or, more likely, an as-yet undetected companion[5] — would readily explain its axisymmetric appearance in the hard-band image (Fig. 9) and the apparent "breakout" of X-ray-emitting plasma beyond the bright rim of near-infrared emission from ionized gas (Fig. 7). Indeed, the morphology of high-velocity Brγ emission is very similar to that of the X-ray emission (Cox et al.). Similarly, both the optical emission and the diffuse, soft X-ray emission from NGC 6543 appear to be point-symmetric (see Fig. 10 and Chu et al. 2001), suggestive of the action of collimated outflows (although Chu et al. ascribe the limb-brightened appearance of the X-ray emission from NGC 6543 to the effects of heat conduction or mixing of shocked plasma with photoionized gas).

BD +30°3639 may be an example of a PN in which heat conduction and/or mixing play a crucial role in determining X-ray morphology. Either mechanism would explain the bright, compact X-ray-emitting region at the eastern rim of the nebula, with heat conduction more naturally explaining its plasma abundances (Soker & Kastner 2003). However, BD +30°3639 and NGC 7027 bear strong resemblances in many fundamental respects (e.g., Soker & Kastner 2003) and, in particular, BD +30°3639 is also known to harbor collimated outflows (Bachiller et al. 2000). Hence the asymmetric appearance of BD +30°3639 at high energy, in comparison with NGC 7027, may be primarily the result of the different line-of-sight inclinations of these two nebulae (Masson 1989; KSVD; see,

[5]It seems unlikely that a moderate-speed (~ 400 km s^{-1}), collimated wind could be driven by the present central star, as such a wind speed is much smaller than the escape velocity from a star of mass of $0.7M_{\odot}$ and radius $0.07R_{\odot}$ (Latter et al. 2000b).

however, Bryce & Mellema 1999, who find that BD +30°3639 more closely resembles the elliptical PN NGC 40). It remains to demonstrate, however, how collimated outflows might produce the off-center X-ray bright spot in BD +30°3639, as the outflows detected by Bachiller et al. do not correspond spatially to this region of X-ray emission.

5. Summary and Conclusions

We have presented and analyzed reprocessed X-ray Chandra X-ray Observatory images of the planetary nebulae BD +30°3639, NGC 7027, and NGC 6543. To maximize the spatial resolution of the images, we employ an event relocation technique that takes full advantage of CXO's exceptional spatial resolution; we estimate that the reconstructed images represent a $\sim 30\%$ improvement in PSF FWHM, over the original images. Energy-resolved images demonstrate that the morphologies of all three nebulae depend sensitively on energy. Whereas NGC 7027 appears clumpiest at low energy and more symmetric at higher energy, BD +30°3639 becomes more one-sided and asymmetric with increasing X-ray energy. Diffuse emission from NGC 6543 is dominated by soft X-rays, with its central point source dominant in the harder energy bands.

With the aid of high-resolution optical and near-infrared H II emission line images, we consider the extent to which nonuniform intranebular absorption affects the X-ray morphologies of these PNs. For both BD +30°3639 and NGC 7027, we find a strong anticorrelation between broad-band X-ray surface brightness and the degree of visual extinction, where the latter is inferred from the spatial distribution of H II line ratios. We conclude that extinction plays an important role in the overall X-ray appearances of these young, dusty, molecule-rich PNs. The PN NGC 6543 has a much smaller and more spatially uniform degree of visual extinction than either BD +30°3639 or NGC 7027, however, so spatially variable absorption does not affect its X-ray morphology.

While extinction is important in determining the X-ray surface brightnesses of BD +30°3639 and NGC 7027, extinction alone cannot explain many important characteristics of the X-ray morphologies of these PNs. In particular, the highly asymmetric appearance of BD +30°3639 and the axisymmetric or point-symmetric appearances of NGC 7027 and NGC 6543 appear to point out intrinsic X-ray emission properties of these nebulae. We conclude that the action of collimated outflows likely dictates the X-ray appearances of at least two of three nebulae studied here, with heat conduction in the presence of magnetic fields potentially playing a more important role in the asymmetric surface brightness of BD +30°3639.

Additional spatially resolved CXO/ACIS and XMM-Newton observations of planetaries are required to better establish the relative importance of the various processes — e.g., collimated outflows, heat conduction, mixing of shock-heated and photoionized plasma — proposed to explain their X-ray morphologies as well as their X-ray luminosities and temperatures. We have demonstrated here that these observations must be accompanied by subarcsecond emission-line imaging in the optical and near-infrared, to unambiguously distinguish between intrinsic and extrinsic processes that can determine the energy-dependent X-ray morphologies of PNs.

The authors wish to thank two anonymous referees for many helpful comments and suggestions. J.H.K. and J.L. acknowledge support for this research provided by NASA/CXO grant GO0–1067X to RIT. N.S. acknowledges support from the US-Israel Binational Science Foundation.

REFERENCES

Arnaud, K. , Borkowski, K. J., & Harrington, J. P. 1996, ApJ, 462, L 75.

Bachiller, R., Forveille, T., Huggins, P. J., Cox, P., & Maillard, J. P. 2000, A&A, 353, L5

Bryce, M., & Mellema, G. 1999, MNRAS, 309, 731

Chu, Y.-H., Guerrero, M. A., Gruendl, R. A., Williams, R. M., Kaler, J. B. 2001, ApJ, 553, L69

Cox, P., Huggins, P.J., Maillard, J.-P., Habart, E., Morisset, C., Bachiller, R., & Forveille, T. 2002, A&A, in press

Frank, A. 1999, New Astr. Rev., 43, 31

Gardiner, T.A., & Frank, A. 2001, ApJ, 557, 250

Graham, J. R., Serabyn, E., Herbst, T. M., Matthews, K., Neugebauer, G., Soifer, B. T., Wilson, T. D., & Beckwith, S. 1993, AJ, 105, 250

Gruendl, R. A., Chu, Y.-H., O'Dwyer, I. J., Guerrero, M. A. 2001, AJ, 122, 308

Guerrero, M. A., Chu, Y.-H., Gruendl, R. A. 2002, A&A, 387, L1

Guerrero, M. A., Chu, Y.-H., Gruendl, R. A., Williams, R. M., Kaler, J. B. 2001, ApJ, 553, L55

Harrington, J.P., Lame, N.J., White, S.M., & Borkowski, K.J. 1997, AJ, 113, 2147

Kastner, J.H., Gatley, I., Merrill, K.M., Probst, R., & Weintraub, D.A. 1994, ApJ, 421, 600

Kastner, J.H., Soker, N., & Rappaport, S., eds. 2000a, "Asymmetrical Planetary Nebulae II: From Origins to Microstructures," ASP Conf. Ser. Vol. 199

Kastner, J. H., Soker, N., Vrtilek, S. D., Dgani, R. 2000b, ApJ, 545, L57 (KSVD)

Kastner, J. H., Vrtilek, S. D., Soker N. 2001, ApJ, 550, L189 (KVS)

Kastner, J. H., Weintraub, D.A., Gatley, I., Merrill, K.M., & Probst, R. 1996, ApJ, 462, 777

Latter, W.B., Dayal, A., Bieging, J.H., Kelly, D.M., Hora, J.L., & Tielens, A.G.G.M. 2000a, in "Asymmetrical Planetary Nebulae II: From Origins to Microstructures," eds. J.H. Kastner, N. Soker, & S. Rappaport, ASP Conf. Ser. Vol. 199, p. 263

Latter, W. B., Dayal, A., Bieging, J. H., Meakin, C., Hora, J. L., Kelly, D. M., & Tielens, A. G. G. M. 2000b, ApJ, 539, 783

Li, J., Kastner, J.H., Schulz, N. S., & Marshall, H. L. 2002, BAAS, 200, 5906

Masson, C. R. 1989, ApJ, 346, 243

Osterbrock, D.E. 1989, "Astrophysics of Gaseous Nebulae and Active Galactic Nuclei," (Mill Valley: University Science Books)

Robberto, M., Clampin, M., Ligori, S., Paresce, F., & Staude, H. J. 1993, A&A, 280, 241

Sahai, R., & Trauger, J.T. 1998, AJ, 116, 1357

Soker, N., & Kastner, J. H. 2002, ApJ, 570, 245

Soker, N., & Kastner, J. H. 2003, ApJ, submitted (posted to astro-ph, July 2003)

Soker, N., & Rappaport, S. 2000, ApJ, 538, 241

Tsunemi, H., Mori, K., Miyata, E., Baluta, C., Burrows, D., Garmire, G. P., & Chartas, G. 2001, ApJ, 554, 496

Tylenda, R., Acker, A., Stenholm, B., & Koeppen, J. 1992, A&AS, 95, 337

Weintraub, D.A., Kastner, J.H., Gatley, I., & Merrill, K.M., 1996, ApJ, 468, L45

This manuscript was prepared with the AAS LaTeX macros v5.0.

Table 1: Event Grade Distributions for Planetary Nebulae Observed by CXO

		NGC 6543		BD +30°3639		NGC 7027	
Event type	FLTGRADE	No.	%	No.	%	No.	%
All	(all)	1755	...	4868	...	306	...
Single-pixel	0	830	47.3	1934	39.7	95	31.0
Two-pixel	2,8,16,64	764	43.5	2233	45.9	161	52.6
Corner-split	10,11,18,22, 72,80,104,208	127	7.2	456	9.4	40	13.1
Selected	0,2,8,10,11, 16,18,22,64, 72,80,104,208	1721	98.1	4623	95.0	296	96.7

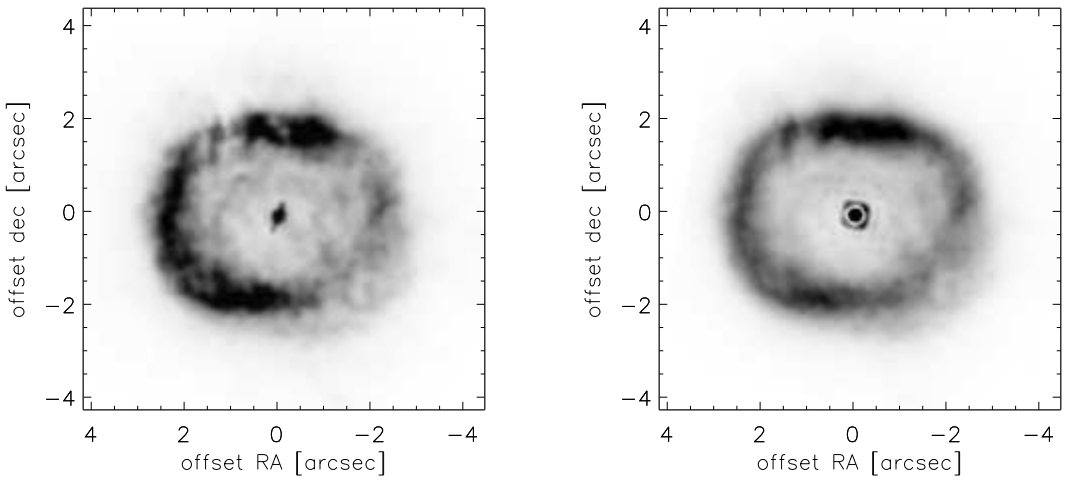


Fig. 1.— *Hubble Space Telescope* Hα 0.6563 μm (left) and Pα 1.87 μm (right) images of BD +30°3639 obtained with WFPC2 and NICMOS, respectively.

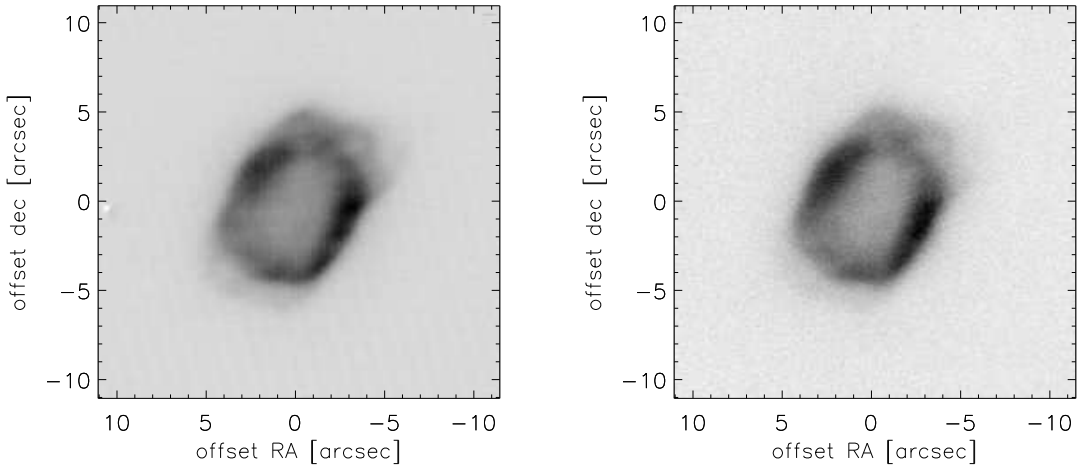


Fig. 2.— Brγ 2.16 μm (left) and Brα 4.05 μm (right) images of NGC 7027, obtained with the Cryogenic Optical Bench on the Kitt Peak 4 m telescope.

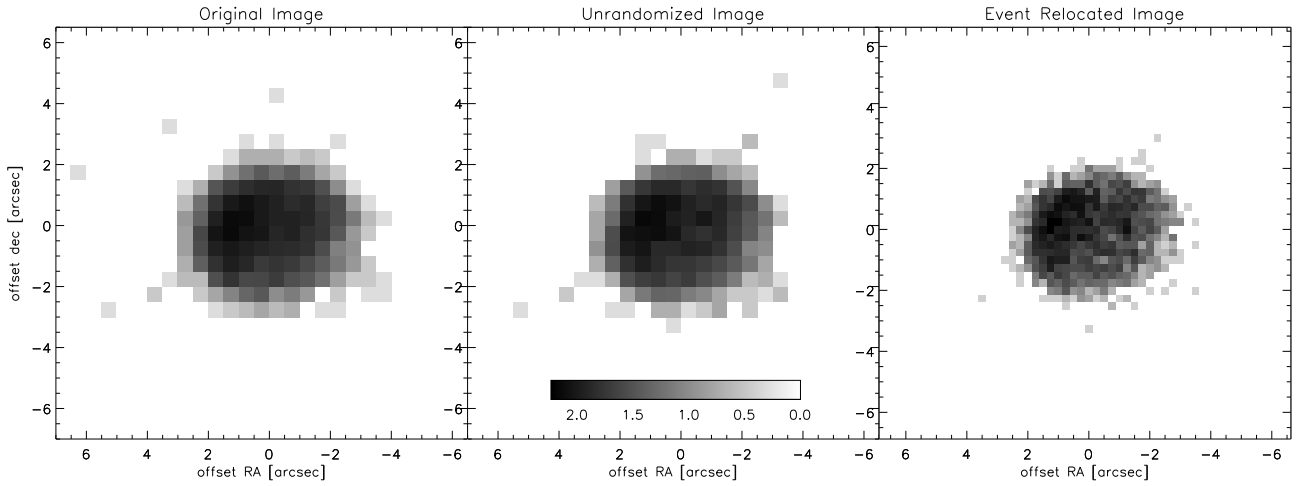


Fig. 3.— Left: CXO X-ray image of BD +30°3639, obtained by binning events before removing position randomization or applying sub-pixel event position corrections. Center: image of BD +30°3639 obtained by binning events after removing event position randomization. Right: image of BD +30°3639 obtained by binning events after removing randomization and applying sub-pixel event position corrections. Images in this and the next two figures are presented in a log scale, with the bars representing the greyscale mapping to log intensity.

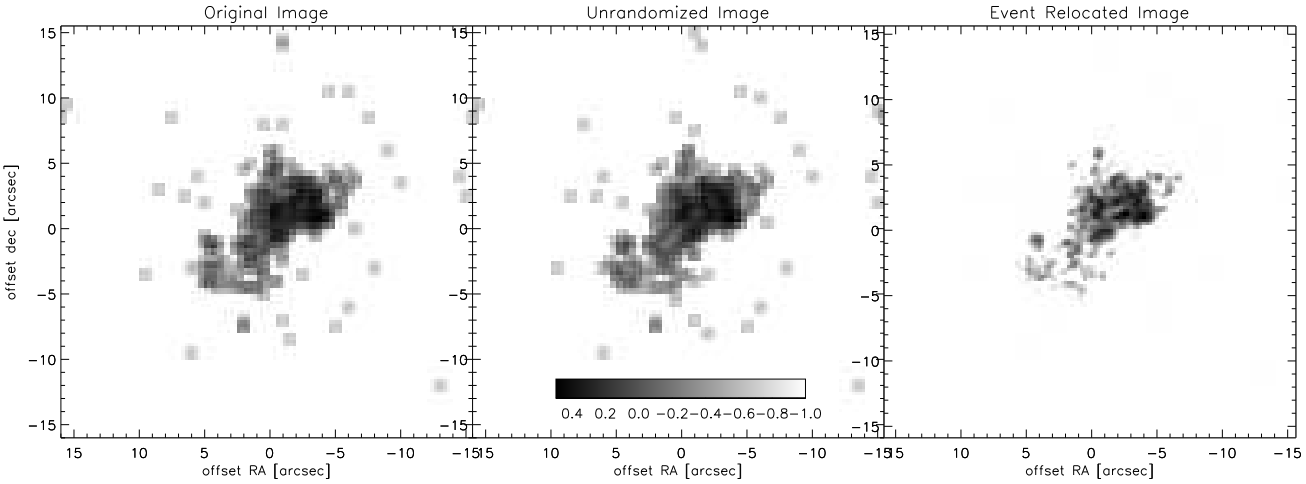


Fig. 4.— Left: CXO X-ray image of NGC 7027, obtained by binning events before removing position randomization or applying sub-pixel event position corrections. Center: image of NGC 7027 obtained by binning events after removing event position randomization. Right: image of NGC 7027 obtained by binning events after removing randomization and applying sub-pixel event position corrections.

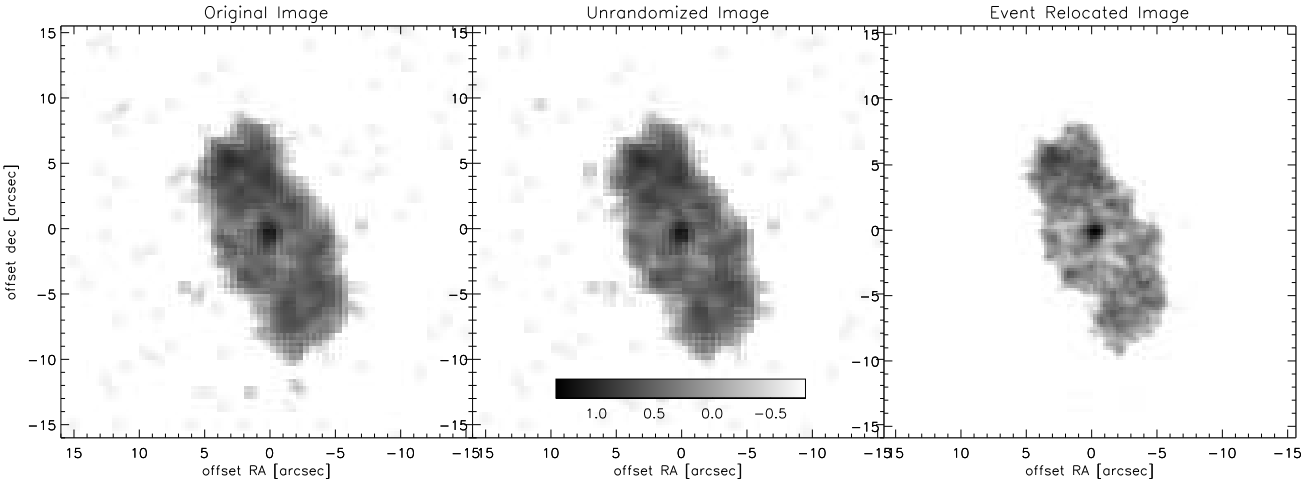


Fig. 5.— Left: CXO X-ray image of NGC 6543, obtained by binning events before removing position randomization and applying sub-pixel event position corrections. Center: image of NGC 6543 obtained by binning events after removing event position randomization. Right: image of NGC 6543 obtained by binning events after removing randomization and applying sub-pixel event position corrections.

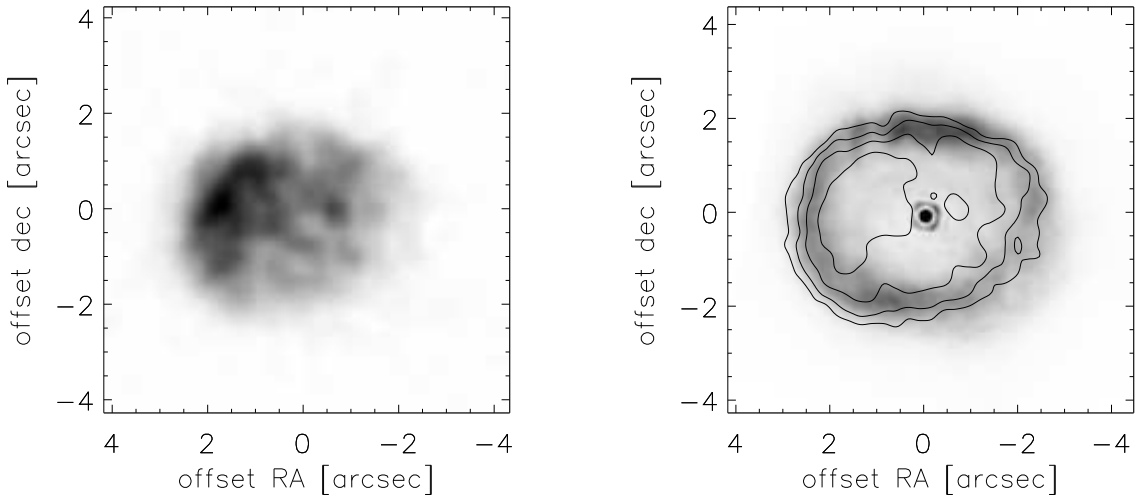


Fig. 6.— Left: Reconstructed, broad-band CXO X-ray image of BD +30°3639. Right: Contours of X-ray surface brightness overlaid on the Pα image of Fig. 1. Contour levels are at 12, 24, 48, and 96 counts arcsec^{-2}. In this Figure and in Fig. 7, the CXO image has been convolved with a Gaussian function with width approximating that of the instrumental point spread function.

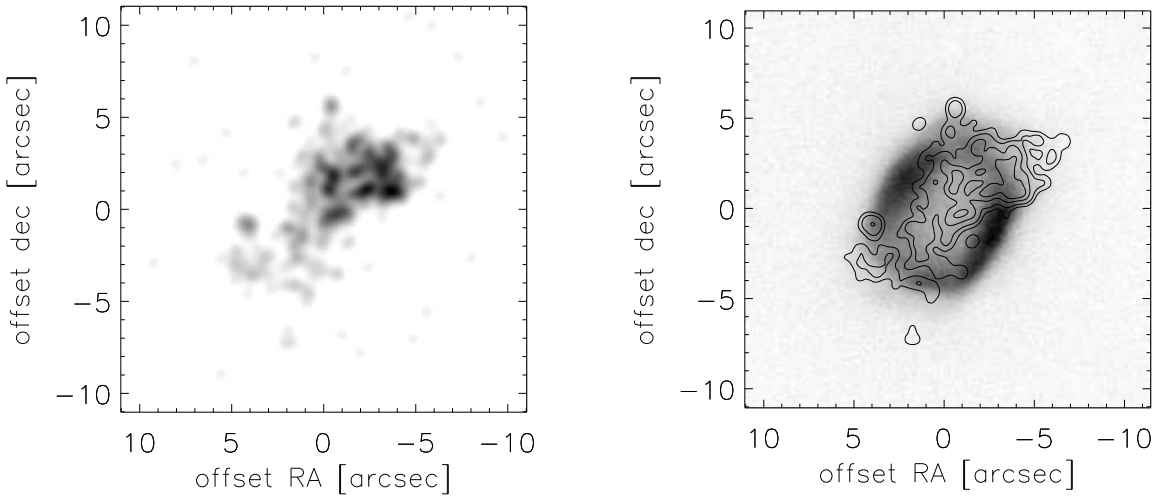


Fig. 7.— Left: Reconstructed, broad-band CXO X-ray image of NGC 7027. Right: Contours of X-ray surface brightness overlaid on the Brα image of Fig. 2. Contour levels are at 4, 8, 16, and 24 counts arcsec^{-2}. In each panel, offset (0,0) corresponds to the position of the central star to $\sim 0.2''$ (as determined from comparison of the Brα image with HST near-infrared imagery; Latter et al. 2000b).

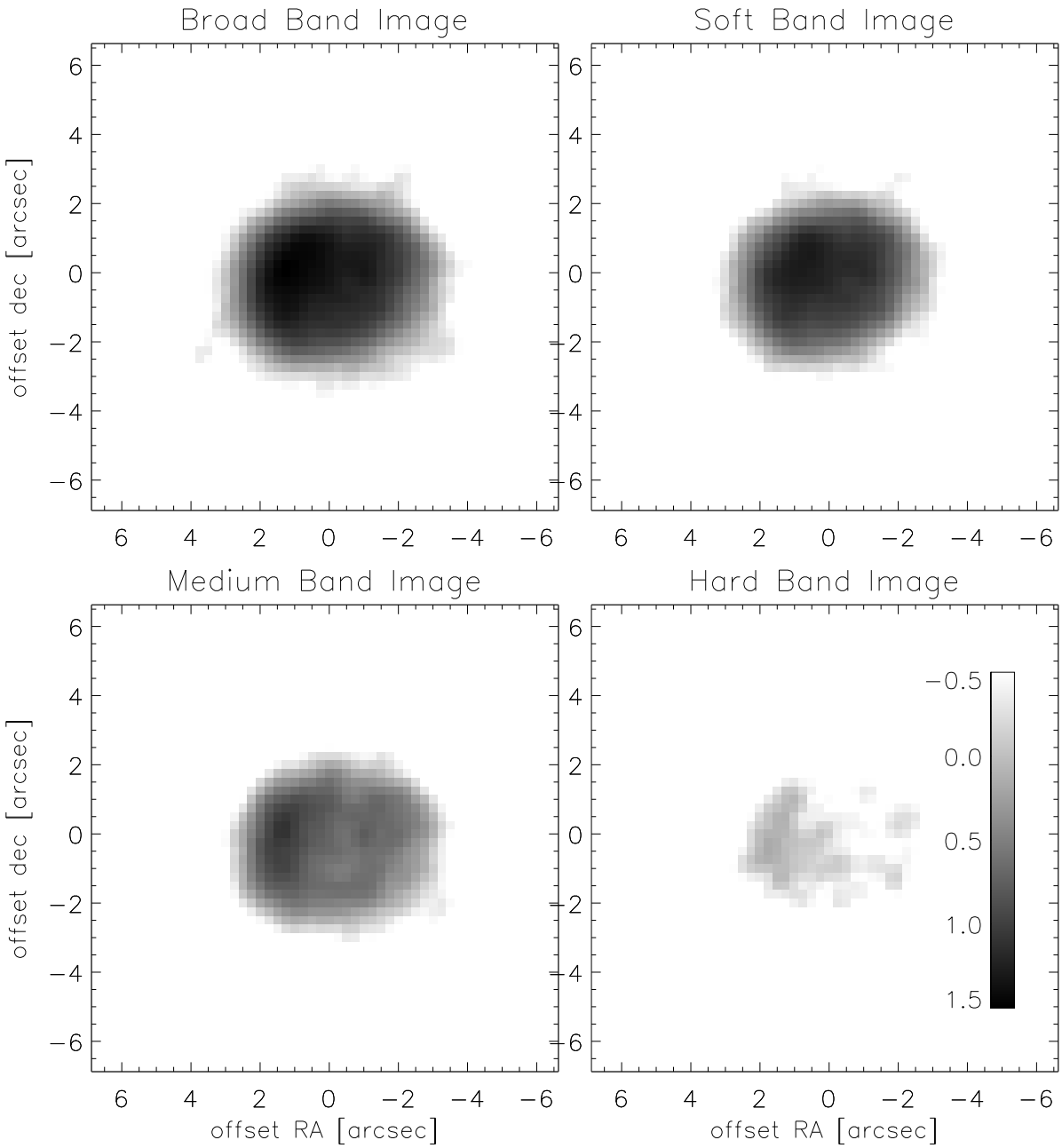


Fig. 8.— Energy-resolved images of BD +30°3639. Upper left: broad-band image, obtained from all events with energies $\leq$ 3.0 keV. Upper right: soft-band image, obtained from events with energies $\leq$ 0.7 keV. Lower left: medium-band image, obtained from events with energies between 0.7 keV and 1.2 keV. Lower right: hard-band image, obtained from events with energies between 1.2 keV and 3.0 keV. Images in this and the next two figures are presented in a log scale, with the bars representing the greyscale mapping to log intensity.

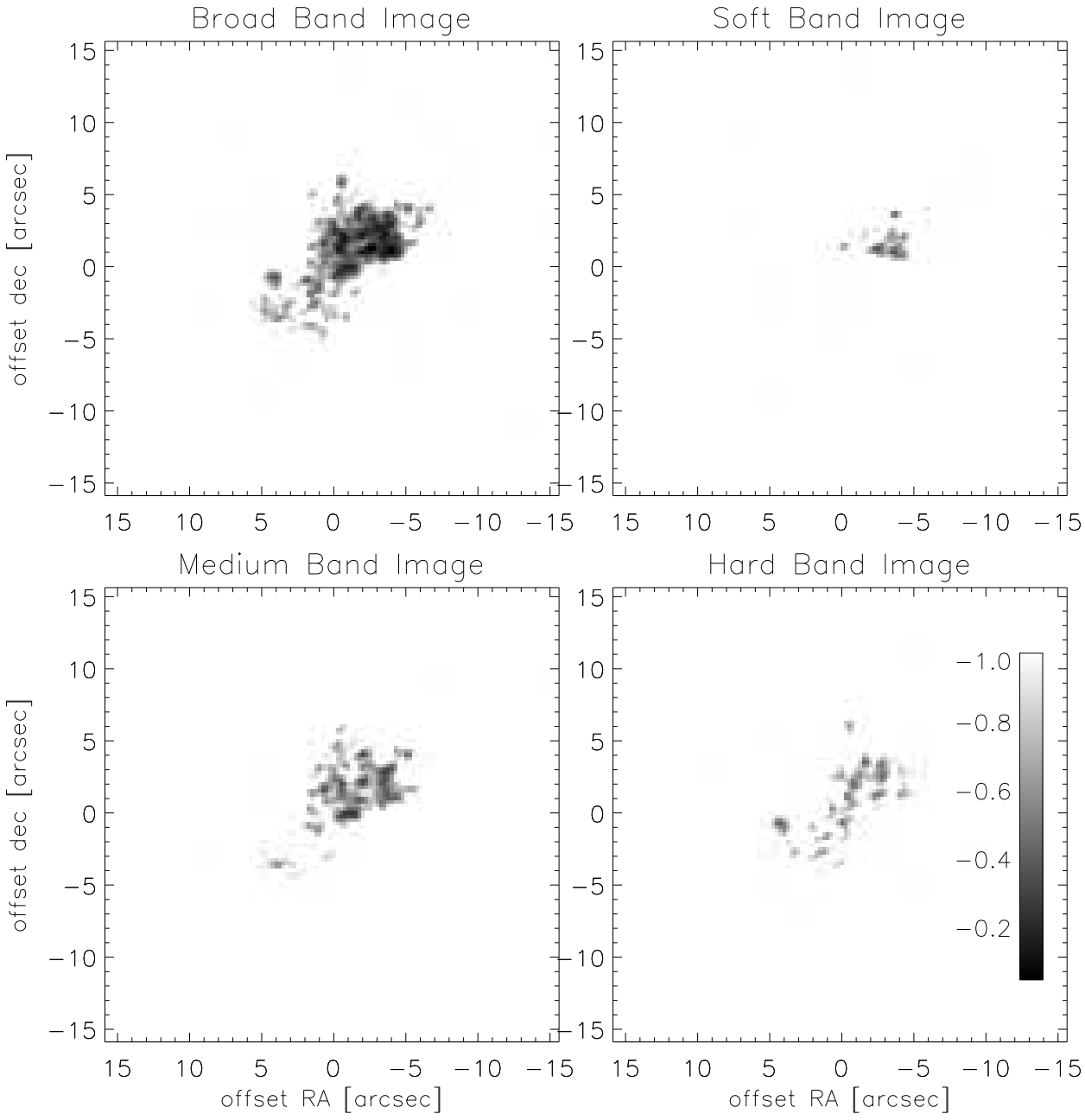


Fig. 9.— Energy-resolved images of NGC 7027. Energy ranges for panels are as in the previous figure.

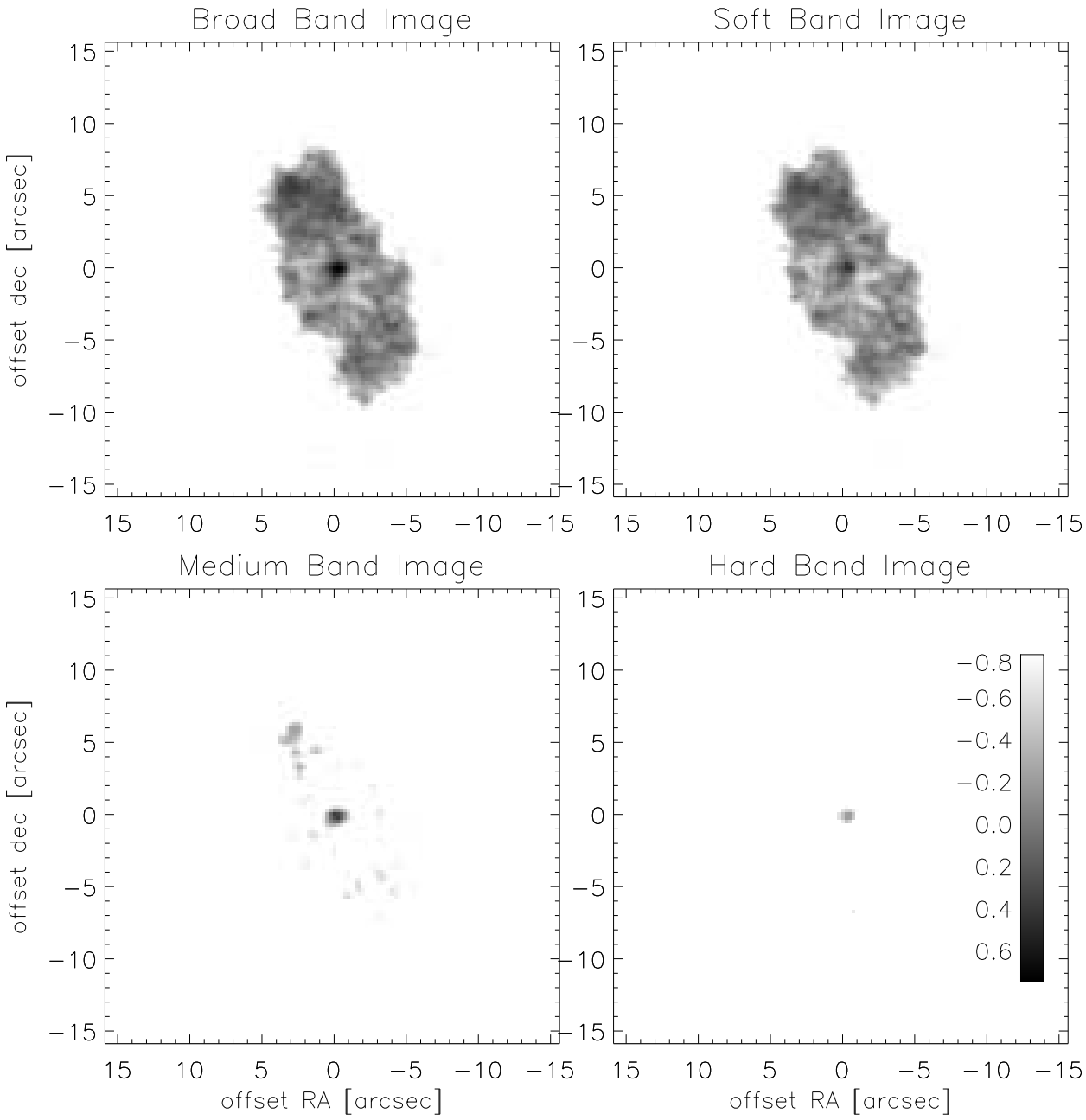


Fig. 10.— Energy-resolved images of NGC 6543. Energy ranges for panels are as in Fig. 8.

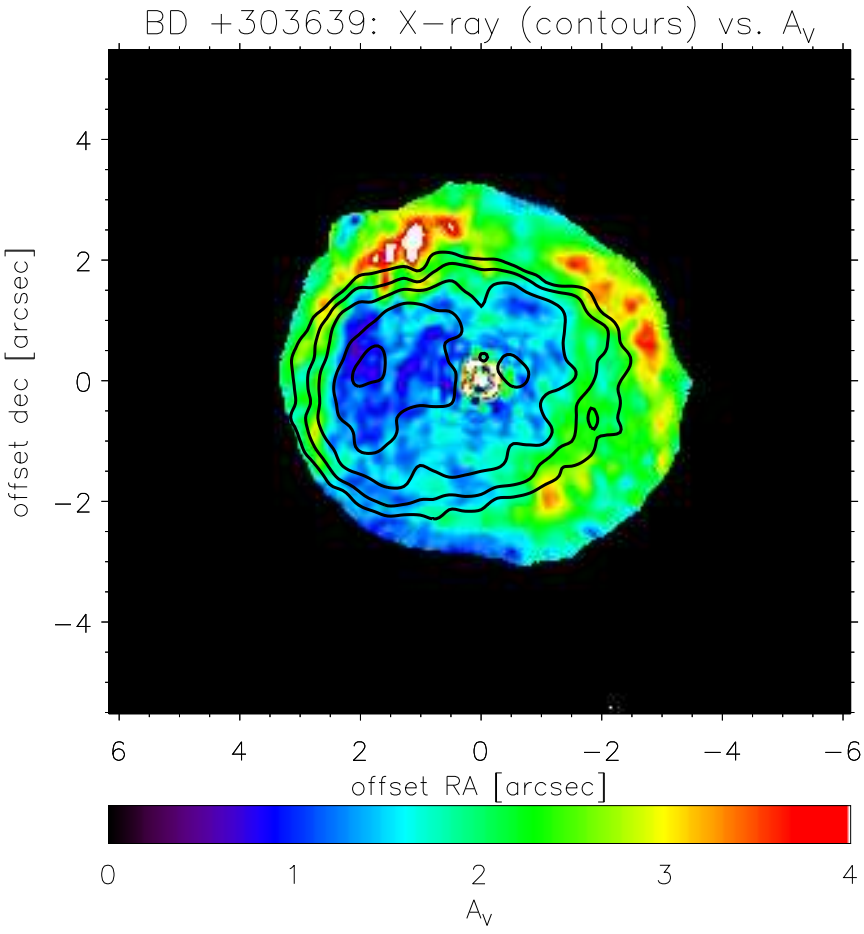


Fig. 11.— Overlay of CXO X-ray image (contours) on extinction map of BD +30°3639 (color).

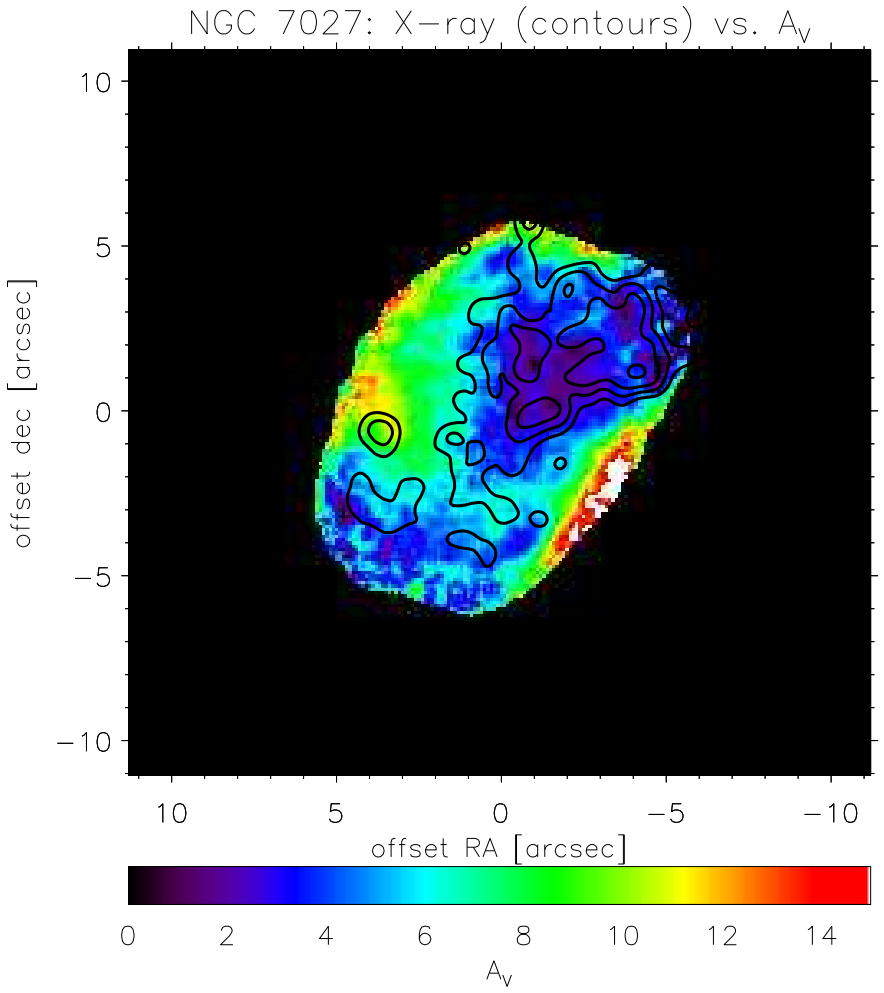
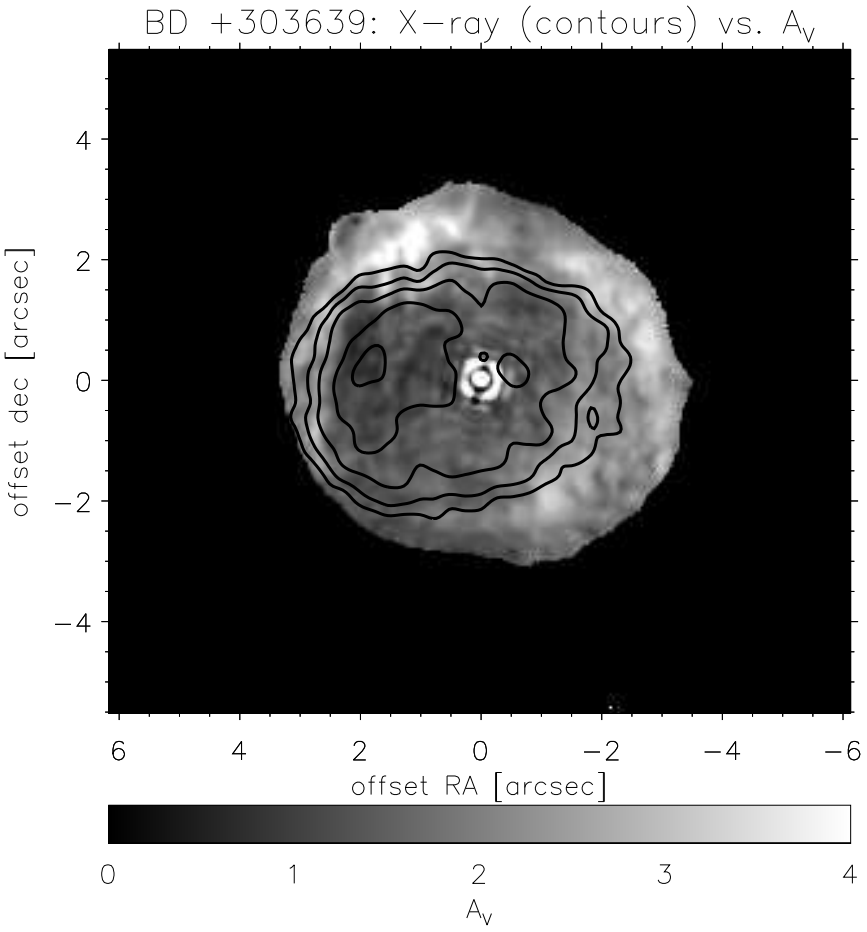
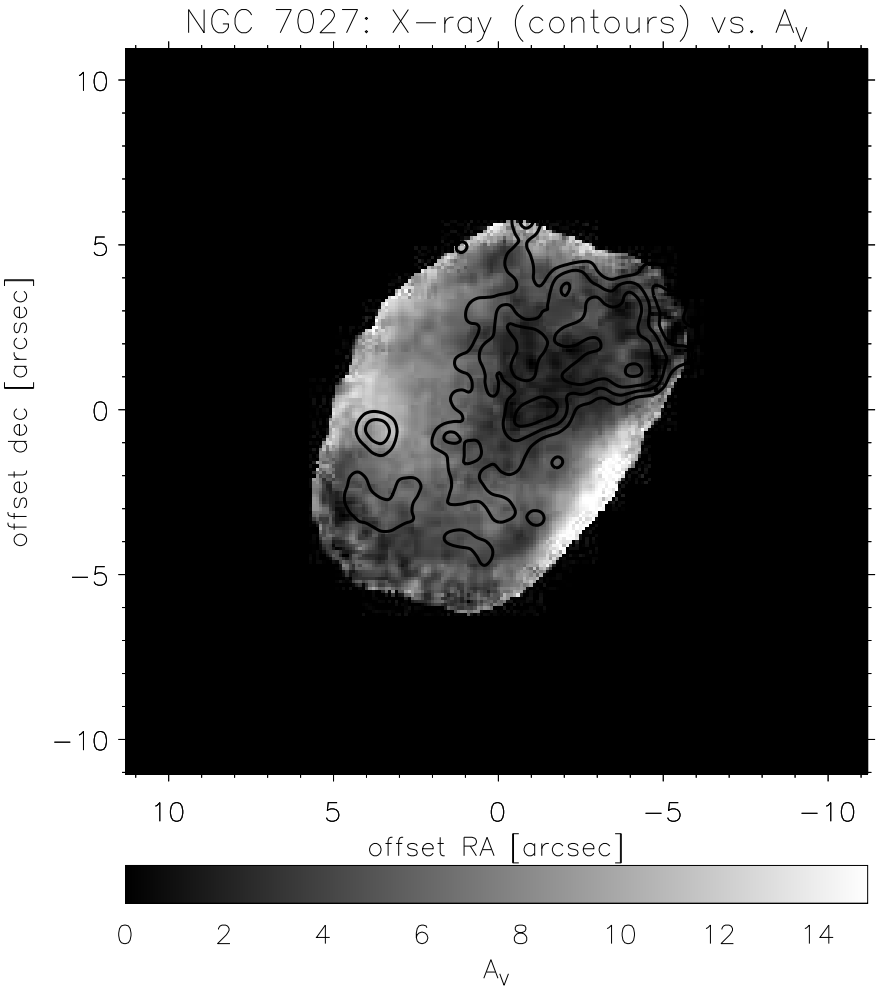


Fig. 12.— Overlay of CXO X-ray image (contours) on extinction map of NGC 7027 (color).


BD +303639: X−ray (contours) vs. A_V
offset dec [arcsec]
4
2
0
−2
−4
6
4
2
0
−2
−4
−6
offset RA [arcsec]
0
1
2
3
4
A_V


NGC 7027: X−ray (contours) vs. A_V
10
5
0
−5
−10
offset dec [arcsec]
10
5
0
−5
−10
offset RA [arcsec]
0
2
4
6
8
10
12
14
A_V